Suppression of helium bubble nucleation in beryllium exposed tungsten surfaces

M.A. Cusentino⬡, M.A. Wood and A.P. Thompson⬡

Center for Computing Research, Sandia National Laboratories, Albuquerque, NM, United States of America

E-mail: mcusent@sandia.gov

CrossMark

Abstract

One of the most severe obstacles to increasing the longevity of tungsten-based plasma facing components, such as divertor tiles, is the surface deterioration driven by sub-surface helium bubble formation and rupture. Supported by experimental observations at PISCES, this work uses molecular dynamics simulations to identify the microscopic mechanisms underlying suppression of helium bubble formation by the introduction of plasma-borne beryllium. Simulations of the initial surface material (crystalline W), early-time Be exposure (amorphous W-Be) and final WBe_2 intermetallic surfaces were used to highlight the effect of Be. Significant differences in He retention, depth distribution and cluster size were observed in the cases with beryllium present. Helium resided much closer to the surface in the Be cases with nearly 80% of the total helium inventory located within the first 2 nm. Moreover, coarsening of the He depth profile due to bubble formation is suppressed due to a one-hundred fold decrease in He mobility in WBe_2, relative to crystalline W. This is further evidenced by the drastic reduction in He cluster sizes even when it was observed that both the amorphous W-Be and WBe_2 intermetallic phases retain nearly twice as much He during cumulative implantation studies.

Supplementary material for this article is available online

(Some figures may appear in colour only in the online journal)

1. Introduction

One of the most challenging aspects of engineering a viable fusion reactor is designing materials that can withstand the the harsh conditions present upon the plasma facing components (PFCs). In particular, the divertor is subject to high fluxes on the order of 10^{24} m^2 s^{-1} of multiple plasma species and high thermal fluxes of 10–20 MW m^{-2} [1]. Currently, tungsten and beryllium have been chosen as materials for the divertor and inner wall, respectively, for the International Thermonuclear Experimental Reactor (ITER). Tungsten's high melting temperature, good thermal conductivity and low sputtering yield make it a prime candidate for the divertor region [2] while

the favorable thermo-mechanical properties and low Z number make beryllium a suitable material for the inner wall [1].

The variety of plasma species (H, He, Be, etc) impinging at the divertor surface leads to microstructural changes which can ultimately affect the performance of the divertor. One of the most striking surface modifications are the nanotendrils that form after helium implantation in tungsten under plasma conditions [1, 3]. Low energy, high flux helium plasmas have been shown to form *fuzz*-like tendrils on tungsten surfaces at temperatures in the range of 1000 K to 2000 K and has been observed in both tokamaks [4] and linear plasma experiments [5–8]. At lower fluences, before fuzz forms, a subsurface network of helium bubbles will form and the growth, rupture

and subsequent surface deformation from these processes are likely linked to fuzz growth over time [3, 7–15]. The main concern of fuzz growth at the divertor surface is the degradation of tungsten material properties such as thermal conductivity [5] and the risk that these structures could easily break away from the surface allowing for tungsten to contaminate and quench the plasma [16].

However, experiments investigating mixed material effects have shown that beryllium deposits can also affect helium nanotendril formation. Beryllium from the first wall can erode and transport to the divertor [17] where experiments have shown that W-Be intermetallics can form [18–20]. One particular set of experiments indicated that increasing levels of Be in the plasma resulted in a lack of fuzz growth [21]. However, beryllium is not the anomalous contaminate material, experiments have shown that helium bubbles will suppress hydrogen blisters [22, 23] while nitrogen implantation leads to the formation of tungsten-nitrides that result in higher hydrogen retention [24, 25]. Clearly, there are synergestic effects between plasma species in tungsten which warrants further study of these mechanisms. Each of these prior studies highlights the physical and chemical changes that the plasma species induce upon PFCs, the present work aims to understand the mechanisms of He retention where Be is present at the divertor surface. Specifically, this work differentiates the structural changes of the W surface that Be deposition causes from the chemical makeup of the surface as it pertains to He retention and bubble formation. This is an important factor in understanding the experimental observations of reference [21] where it is unclear the mechanism by which the Be affects He retention. The following sections detail our simulation methods that produce realistic PFC environments followed by our detailed analysis of the subsequent He implantation before drawing conclusions on these mixed material effects.

2. Methods

To understand the role of Be in He retention, we have designed our simulation efforts to contrast different *stages* of the PFC during Be deposition. These stages correspond to the pristine BCC W ([001] surface normal) surface, early time ($\sim$ns) Be exposure and a thermodynamically stable WBe_2 intermetallic (C14 Laves Phase). Preparation of the early-time Be exposed sample is directly simulated in MD via 75 eV Be implantation to a fluence of 1.4×10^{20} m^{-2}. Experimental results show the formation of ordered intermetallic structures but directly reproducing these phases following energetic Be implantation is beyond the timescales of direct MD simulations without becoming prohibitively computationally expensive. The C14 Laves phase was chosen since it has the lowest formation energy predicted by the potential used in this work [26]. The Be exposed (early-time) sample results in a mixed W-Be amorphous layer within the first 2 nm of the surface that has some structure that is however trending toward an ordered intermetallic. To contrast the effect of this structural disorder, we have also constructed a W surface that has the first 2 nm melted and quenched to yield a similarly amorphous

near-surface layer as the Be exposed sample. A comparison of each surface type is supplied in the supplemental material (https://stacks.iop.org/NF/60/126018/mmedia) as a set of W-W radial distribution functions.

For each prepared surface, two styles of helium implantation simulations were performed. The first of which involved repeated, single helium implantations at an initial kinetic energy of 100 eV in order to generate a depth distribution profile. The second measures the cumulative helium implantation up to a fluence of 2.8×10^{19} m^{-2} at the same implantation energy in order to study the dynamics of helium bubble formation within the different surface structures.

All molecular dynamics (MD) simulations were performed using the Large-scale Atomic/Molecular Massively Parallel Simulator (LAMMPS) [27] code. Each simulation cell ($\approx 6 \times 6 \times 12$ nm) has a (001) surface exposed along the elongated axis and is pre-heated to 1000 K using a Langevin thermostat [28, 29]. To simulate the helium implantation, running in the micro-canonical ensemble, a single helium is placed 1 nm above the surface with randomly generated lateral coordinates and given 100 eV of kinetic energy directed perpendicular to the surface. A variable timestep was used to resolve these high energy collisions. In addition, the surface opposite of the He implantation was fixed in space in order to prevent an accumulation of center-of-mass motion for all simulations. For the single implantation case, the simulation was evolved for 3 ps of the implantation, after which the depth of the helium atom was recorded. A total of 1000 individual simulations were performed for each surface morphology, recording the depth of the lone He implanted each time. Helium atoms were identified to be at interstitial or substitutional sites using Voronoi analysis implemented in OVITO [30], where the Voronoi indices distinguish the resultant site where He is captured.

For the cumulative helium implantation simulations, a new atom with an energy of 100 eV was implanted every 10 ps resulting in a flux of 2.8×10^{27} m^{-2} s^{-1}. In this case, a thermostat was briefly turned on at the end of the 10 ps to maintain the temperature at 1000 K.

Along with the W-W, W-Be and Be-Be interactions that are captured by the Spectral Neighborhood Analysis Potential (SNAP) of Wood *et al* [26] the remaining He interactions are represented as pair-wise functions. For these He pair interactions, we used existing potentials except for Be-He where we developed a new pair potential. The pair potentials used for the remaining helium interactions includes a W-He pair potential developed by Juslin and Wirth [31] along with a He-He pair potential developed by Beck [32] and further modified by Morishita *et al* [33] for short range interactions. There is no existing Be-He potential so we developed a new pair potential following the method used by Juslin and Wirth for the W-He potential. Namely, the pair potential consists of a ZBL at short range, a sixth order polynomial at moderate range and a decaying exponential term at long range. The parameters were fit to a set of density function theory (DFT) data of defect formation energies of helium in beryllium [34]. The new Be-He potential well reproduces these formation energies and further details on the potential and fitting methodology can be found in the supplemental material.
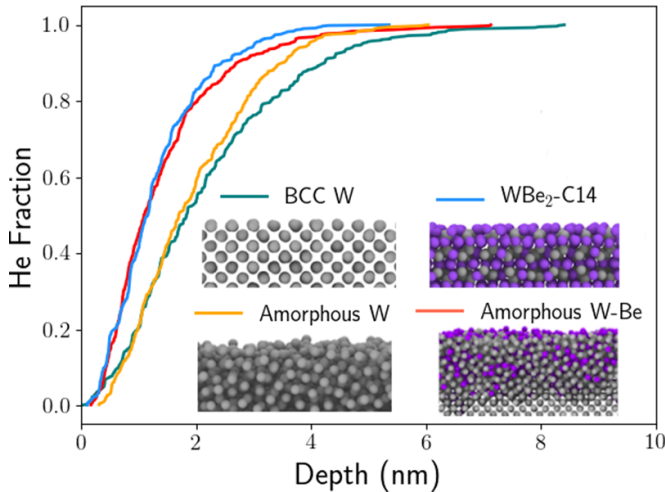
Figure 1. Cumulative depth distribution for an ensemble of individual helium implantation events in different materials: crystalline BCC tungsten (green), amorphous W-Be (red), the WBe$_2$ C14 phase (blue) and amorphous tungsten (purple). For each material, data represents the fraction of post-implantation He atoms located within a given depth from the surface. For each material, depth is measured with respect to the top-most atoms. The inset images depict the surface structure for each material where grey and purple represent tungsten and beryllium respectively.

3. Results

3.1. Helium implantation depth profiles

To investigate the effects of beryllium on the initial helium implantation, a series of single, 100 eV, helium implantations were performed for the different tungsten and tungsten-beryllium surface structures previously described. These He depth profiles are plotted in figure 1 and each surface morphology is also displayed as an inset where grey and purple atoms represent the tungsten and beryllium atoms, respectively. For the pristine BCC W, the depth profile is consistent with previous MD simulations using empirical interatomic potentials [35, 36], which is that nearly all He is captured in the first 10 nm at this implantation energy. However, the depth profile for WBe$_2$ and amorphous W-Be cases are shifted towards a shallower depth profile. About 80% of the helium atoms implant within the first 2 nm in the beryllium cases but only 50% of the He atoms implant at the same depth in crystalline tungsten. Clearly the presence of the beryllium has greatly shifted the depth profile closer to the surface, while surface disorder plays a more subtle role as evidenced by the mild difference between crystalline and amorphous tungsten.

A simple explanation for the shallow depth profiles where Be is present at the surface can be the momentum exchange of the energetic He and (relatively) stationary surface atoms is more evenly shared where colliding particles are similar in mass. This would result in more disorder in the surface structure, since surface Be would recoil more severely than W. On the other hand, the amorphous nature of the W-Be mixed layer lacks ordered channels that would be a pathway for helium to penetrate deeper into the bulk. These two competing effects are contrasted by the WBe$_2$ C14 intermetallic case and the amorphous tungsten case relative to the amorphous W-Be interface. The intermetallic depth profile mimics the profile for the amorphous W-Be case fairly well at all depths, with only <5% difference at depths below 2 nm . The amorphous tungsten case more closely follows the crystalline tungsten case, with a slight deviation past 3 nm where fewer atoms atoms penetrate deeper in the amorphous case. It appears that the shallow depth profile for the amorphous W-Be case is more likely due to the presence of beryllium as opposed to the disordered nature of the mixed W-Be layer. Another confirmation of this is that the two cases with Be present have much higher absorption ratio of helium than the pair of pure tungsten surfaces. For the amorphous W-Be and WBe$_2$ intermetallic surfaces, 49.3% and 60.5% of the total helium atoms implanted compared to only 38.9% and 36.9% for crystalline tungsten and amorphous tungsten. Again, the result of the amorphous W-Be case is closer to the WBe$_2$ intermetallic case as opposed to either of the two tungsten cases.

The He depth distribution results indicate that the presence of beryllium in tungsten greatly affects the initial interaction of helium with the divertor surface. The higher percentage of helium residing near the surface indicates that further penetration into the bulk would be difficult and subsequent bubble formation will be suppressed due to low-barrier He escape from the near-surface regime. Conversely, the higher helium retention is a cause for concern because this will have the opposite effect allowing helium bubbles to form more easily. These initial results warrant further investigation into how the difference observed in initial implantation into tungsten will affect further helium diffusion and bubble nucleation when beryllium is present.

3.2. Sub-surface helium bubble formation

In addition to the initial implantation depth, a set of cumulative He implantation simulations will further track the effect of helium diffusion and bubble nucleation over time. Since the results of the amorphous W surface thus far were very similar to the crystalline W surface [36], we will only compare to the crystalline W case for clarity. Snapshots of the helium distribution at the end of the 10 ns simulations are shown in figure 2 for each of the remaining three surface conditions. Only the helium atoms, depicted in blue, are shown in the lower panels. For the crystalline tungsten case (figure 2(*a*)), a coarse distribution of bubbles forms within 1-2 nm of the surface with larger helium bubbles forming deeper into the material, present up to 11 nm into the sample. There is a distinct gap in the helium distribution at around 4 nm where little to no He resides. This is due to a preferential drift diffusion which drives helium to migrate towards and escape from the surface [37, 38]. This effect has similarly been observed in previous MD work including large-scale simulations of helium implantation in tungsten [38]. This helium bubble distribution is typical of helium implantations in W, given previous MD simulations [13]. In contrast, both surfaces with beryllium present by visual inspection have a distinctly different helium distribution at the end of the simulation. For the WBe$_2$ surface, the helium remains within the first 4 nm of the surface and are relatively
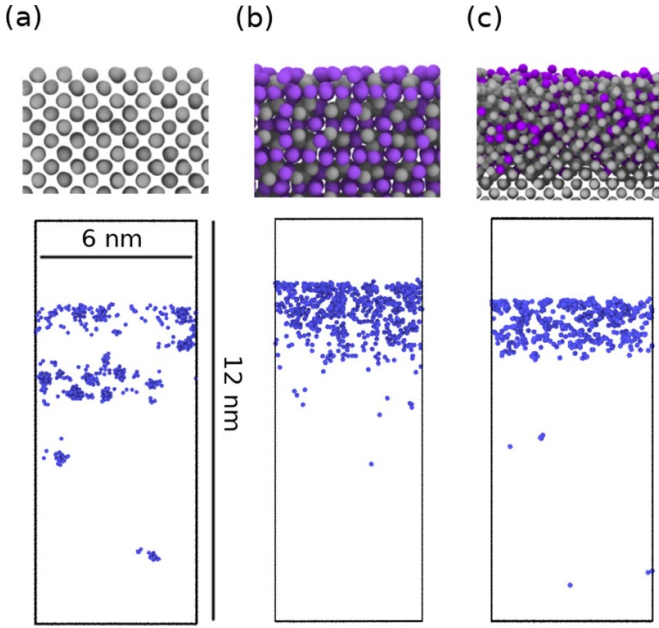
Figure 2. Atomistic snapshots of the cumulative helium implantation simulations at a fluence of 2.8×10^{19} He m^{-2} for (*a*) crystalline BCC tungsten, (*b*) WBe$_2$ C14 intermetallic and (*c*) amorphous W-Be. The top images depict top views of each surface, while the bottom images depict side views showing only the helium atoms. The grey, purple and blue atoms represent tungsten, beryllium and helium respectively. Upper most He atoms reside just below the surface in each panel, see figure 1.

evenly distributed throughout this region. Some lone He are observed past this depth, but no helium clusters form deep into the material as was seen in the crystalline tungsten case. For the amorphous W-Be surface, He is again evenly distributed throughout the first 2 nm, which is where the mixed W-Be layer was formed. Furthermore, there is a clear delineation where the mixed W-Be layer meets the ordered W bulk and there are very few helium atoms that have migrated past the W-Be layer. However, unlike the ordered intermetallic case, there is some helium clustering deeper into the bulk that are comparable to the crystalline tungsten surface albeit on a smaller scale. Both the WBe$_2$ and amorphous W-Be cases display a distinctly different distribution of helium atoms within the material. While the amorphous W-Be case does have some similarities to the crystalline tungsten case deep in the material, it much more closely resembles the WBe$_2$ case in its' net behavior.

To supplement the visual observations, the helium bubble size distribution was quantified and plotted in figure 3(*a*) as the fraction of the total helium atoms as a function of cluster size. The cluster size analysis was performed in OVITO [30] using a cluster cutoff radius of 3 Å. The quantified size distributions confirm the visual observations, the presence of beryllium leads to smaller helium bubble sizes. All three surfaces have similar distributions for cluster sizes of 5 or less, with about 50% of the total helium atoms in each of the three cases residing in smaller sized clusters. However, the distributions at larger cluster sizes vary strongly whether beryllium is present or not. For the surfaces with beryllium, half of the helium

atoms are located in moderately sized clusters ranging in size from about 5 to 10 helium atoms. Unlike the crystalline tungsten surface, there are no helium clusters that are larger than 16 atoms in either the amorphous W-Be or WBe$_2$ intermetallic case. In contrast, clusters of up to a size 30 are observed in the crystalline tungsten case which are of concern given large stresses these bubbles exert on the lattice, which ultimately leads to rupture and deterioration of the divertor surface. The distribution is also much coarser for the crystalline tungsten case due to having a few larger sized clusters as opposed to many moderately sized clusters. For instance, the total number of clusters is much higher for the beryllium cases with a total of 182 and 172 clusters for the WBe$_2$ and amorphous W-Be cases while the crystalline tungsten case has only a total of 85 individual clusters. While the smaller clusters tend to be near the surface in the crystalline tungsten case, the larger clusters tend to be deeper in the tungsten bulk as confirmed by figure 3(*b*) and the visualizations in figure 2.

The cluster size distributions show a sharp contrast between the the cases with and without beryllium present and is especially noteworthy when also comparing the helium retention between the three cases. The amorphous W-Be and WBe$_2$ intermetallic cases have a high helium retention of 49.3% and 67%, respectively, while the crystalline tungsten case is much lower with a helium retention of 37%. This retention value accounts for helium that has implanted into the material and has not diffused back to the surface to desorb. While the helium retention is significantly higher when beryllium is present, there are substantially smaller helium bubbles present. The largest helium bubbles in the crystalline tungsten cases is twice the size of the cases when beryllium is present despite the helium retention being lower.

The depth distribution of these cumulative He implantations are quantified and plotted in figure 3(*b*) again displaying a sharp contrast between the crystalline tungsten and mixed material surfaces. For crystalline tungsten, about 40% of the helium atoms reside in the first 2 nm of the material. There is a large jump in the distribution at about 6 nm which is caused by the modified trap mutation that occurs near the surface [37] that forces the helium to drift back towards the surface. Between 6 and 12 nm there are a few other smaller jumps that represent the large clusters in the latter half of the simulation cell. Overall, the depth distribution is fairly smooth within the first 2 nm but becomes coarser deeper into the material due to the formation of larger sized helium bubbles that form. In comparison, almost 80% of the helium atoms are located within the first 2 nm in the amorphous W-Be and WBe$_2$ intermetallic cases, about twice that of the crystalline tungsten case. In addition, virtually all the helium atoms are located within the first 4 nm of the surface with the exception of a few helium atoms in the amorphous W-Be case that are located around 8 nm. The curves are also smoother for these two cases due to the higher concentration of smaller bubbles located in the near surface region. For the amorphous W-Be surface, there are two slight increases in the depth profile at about 1.5 nm and 2.5 nm. This indicates that the initial shallow depth profile will persist over time and helium does not diffuse away from the surface on timescales accessible to these MD simulations.
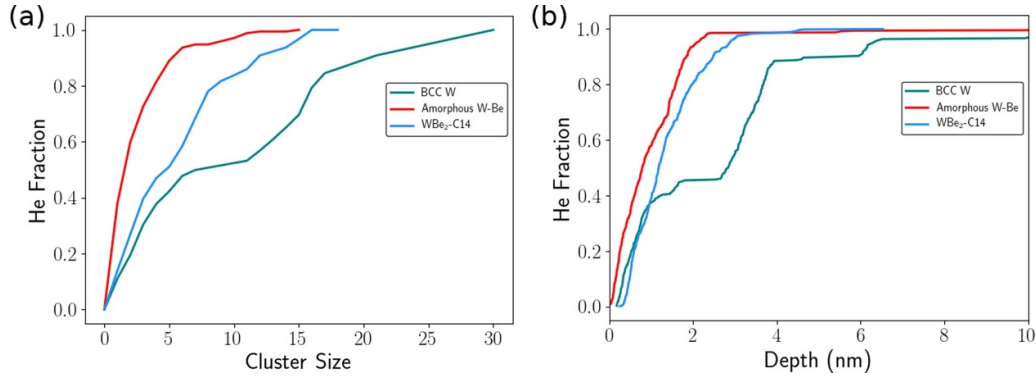
Figure 3. Fraction of helium atoms in the simulation as a function of (*a*) bubble size and (*b*) depth. Green, red and blue represent the helium implantation case for crystalline tungsten, the beryllium deposition simulation and the C14 WBe$_2$ intermetallic.

4. Discussion

The results shown here are consistent with observations from Be exposure experiments conducted at PISCES [21], in particular demonstrating that Be present at the tungsten surface can disrupt He implantation prior to the formation of ordered W-Be intermetallic phases. However, we lack a mechanistic understanding of how these atomistic observations affect fuzz formation at the divertor surface. It is the formation of highly over-pressurized He bubbles within the tungsten lattice that drives the destructive transformation of the surface over time. In crystalline tungsten, helium bubbles nucleate by the initial formation of small mobile interstitial clusters which diffuse and grow large enough until they displace a W lattice atom to form a helium-vacancy (He$_n$V) complex. This phenomenon can be broken down into two key components that can be captured within MD: the energetics of initial He cluster and He$_n$V formation and the migration rate of additional He within the lattice leading to the growth of large clusters or bubbles. Understanding the mechanisms by which He clusters can form, become stable within the lattice and further trap additional He is key to understanding fuzz growth in PFCs.

One observation requiring further examination is that both the ordered and disordered W-Be surfaces capture He at a higher rate than crystalline tungsten, but fail to form large He clusters. Given the simple, pair-wise repulsive potentials that were used to model W-He, Be-He and He-He interactions, we cannot conclude that the higher absorption ratios or differences in clustering are due to weak attractive interactions. A plot demonstrating this purely repulsive nature for all He interactions is provided in the Supplemental Material. The increased absorption ratio can be partially explained by the higher energy transfer in elastic collisions between He and Be atoms, due to the smaller mass ratio compared to W atoms. Using a simple single elastic collision argument [39], the maximum kinetic energy transfer of a He atom colliding with a Be atom is 85.2% of the incident kinetic energy, whereas it is only 8.4% in the case of a W atom, indicating that beryllium is much more efficient at slowing down the incident helium atoms.
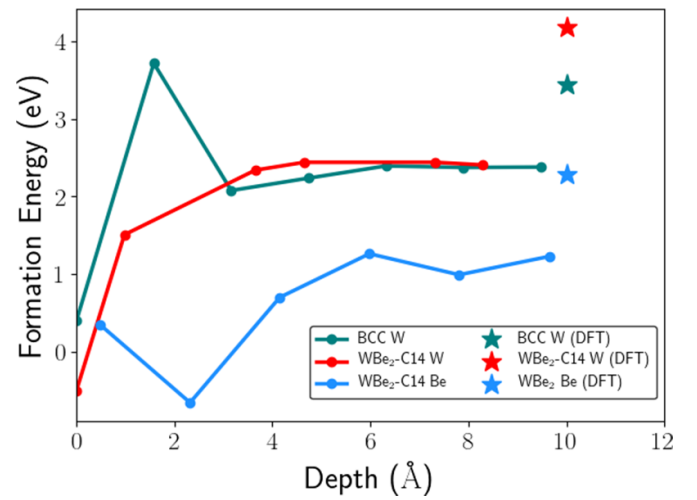
Figure 4. Vacancy formation energy as a function of depth. Green, red and blue represent crystalline BCC W, tungsten in WBe$_2$ C14 intermetallic and beryllium in WBe$_2$ C14 intermetallic.

After the initial implantation event, a He atom can migrate through the solid via interstitial sites or it can displace a W atom creating a vacancy where it becomes trapped. For the ordered surfaces studied here (crystalline W, WBe$_2$ intermetallic) we have calculated the energy to form a vacancy as a function of distance from the surface, displayed in figure 4. In the case of WBe$_2$, one can remove either W or Be from a lattice site. Correlated to this data, it was shown in figure 3(*b*) that ~80% of the captured He resides within the first 2 nm of the intermetallic and within the first 3 nm of crystalline W. These depths correspond to the largest differences in the observed vacancy formation energy, up to a ~4 eV difference.

Therefore it is not surprising that 100% of the singularly implanted He at 100 eV was found to occupy interstitial sites in crystalline W, while only 88% interstitial He was observed in the ordered intermetallic, with the remaining 12% occupying vacancies formed by displacing a W or Be lattice atom. The high energy required to form a vacancy in crystalline tungsten during implantation is consistent with previous the observation that He clusters will form on interstitial sites before displacing

nearby lattice atoms, a process called trap mutation. [13, 40] Of course the rate that trap mutation and bubble growth can progress is limited by the diffusion of He through the lattice, through the connected interstitial sites in the lattice.

To quantify the diffusivity difference between the two ordered surfaces, small periodic (bulk) samples of crystalline W and WBe$_2$ were initialized at 1000 K with a lone interstitial He. Over 30 ns the mean squared displacement of the He atom was tracked and resulting diffusivities of 1.8×10^{-10} m^2 s^{-1} and 1.2×10^{-8} m^2 s^{-1} for WBe$_2$ and crystalline W were measured, respectively. This nearly one-hundred fold decrease in He diffusivity in the intermetallic phase further explains the lack of large bubbles observed in the presence of Be and the subsequently suppression of fuzz growth because the formation of highly over-pressurized bubbles cannot occur as readily [41]. A reduction in diffusivity also explains the similarity in the He depth distributions in figures 1 and 3(*b*) where Be is present, while crystalline W progresses in time toward a stepped depth distribution due to diffusion driven coarsening of the clusters. The stepped depth profile for W in 3(*b*) signifies the growth of larger helium clusters in the material which is accelerated compared to the cases with beryllium due to the higher diffusivity in W.

Again, the MD observation that more He is captured in the early (amorphous W-Be) and late time (WBe$_2$ intermetallic) Be exposed surfaces does not intuitively explain the suppression of fuzz growth. However, the lack of He clustering within the lattice in favor of more uniformly dissolved He can still result in large pressures that can cause cracking or blistering of the divertor surface. If we take the cumulative He deposition simulations described in figure 2 and continue the simulation without implanting He, the residual lateral stresses on the sample will be indicative of the eventual mechanical response at the divertor surface. Comparing the pre- and post-He exposed BCC-W surface, the He clusters were observed to apply 0.57 GPa of in-plane compressive stress on the lattice. Comparatively, the dissolved He in the WBe$_2$ lattice results in 1.72 GPa of in-plane tensile stress, indicating a significant out-of-plane (surface normal) relaxation due to the additional He. For completeness, the amorphous W-Be surface displays 0.50 GPa in-plane tensile stress relative to the pristine crystalline W surface once He was cumulatively implanted. These results are certainly sensitive to the crystallographic orientation used as the surface normal direction, which warrants further study of the mechanical response of divertor materials due to dissolved He. However, the result is clear that these mixed material divertor surfaces have drastically different mechanical responses than the base W surfaces. While these simulations do not directly capture experimental length and time scales, the fundamental changes in helium behavior due to the presence of beryllium in tungsten surface materials, specifically helium retention, depth distribution and bubble size distribution observed in this work indicate a clear alteration in the initial processes leading to fuzz growth.

5. Conclusions

It was observed that helium implantation into crystalline W versus both amorphous and ordered W-Be surfaces indicates a stark difference in helium distribution, retention and bubble sizes. Helium resides much closer to the surface in the W-Be systems, with 80% located within the first 2 nm as opposed to just 45% in pure tungsten for He implanted at 100 eV. In addition, while the helium retention is about twice as high in W-Be surfaces, the helium bubble distribution is skewed towards smaller sizes, with the largest bubble size in pure tungsten being about twice that in W-Be systems. The differences in helium bubble distribution leads to a drastic reduction in compressive stress in the lattice where beryllium is present, indicating that the main driver for fuzz growth, the formation of overpressurized helium bubbles, is suppressed in these mixed materials system. These results indicate the significant effects of plasma borne contaminants present at plasma facing components and highlights the need to shift modeling and simulation efforts toward these complex systems. Furthermore, this work exemplifies the need to adapt widely accepted heuristics of when and how fuzz growth will be initiated in a fusion reactor where one can reasonably expect deviations from pristine divertor surfaces. There exists a need for further examination of two key questions raised by this work, i) how does the transition from early time Be exposure (resulting in amorphous W-Be mixtures) toward ordered intermetallic phases progress and ii) what is the equivalent of the crystalline tungsten trap mutation mechanism in these W-Be mixed materials.

views of the U.S. Department of Energy or the United States Government.

ORCID iDs

M.A. Cusentino ⓘ https://orcid.org/0000-0001-9505-6442
A.P. Thompson ⓘ https://orcid.org/0000-0002-0324-9114

References

[1] Federici G. *et al* 2001 Plasma-material interactions in current tokamaks and their implications for the next step fusion reactors *Nucl. Fusion* **41** 1967–2137

[2] Pitts R.A. *et al* 2013 A full tungsten divertor for ITER: Physics issues and design status *J. Nucl. Mater.* **438** S48–S56

[3] Hammond K.D. 2017 Helium, hydrogen and fuzz in plasma-facing materials *Mater. Res. Express* **4** 104002

[4] Wright G.M. *et al* 2013 Comparison of tungsten nano-tendrils grwon in Alcator C-Mod and linear plasma devices *J. Nucl. Mater.* **438** S84–S89

[5] Kajita S., Takamura S., Ohno N., Nishijima D., Iwakiri H. and Yoshida N. 2007 Sub-ms laser pulse irradiation on tungsten target damaged by exposure to helium plasma *Nucl. Fusion* **47** 1358–66

[6] Iwakiri H., Yasunaga K., Morishita K. and Yoshida N. 2000 Microstructure evolution in tungsten during low-energy helium ion irradiation *J. Nucl. Mater.* **283-287** 1134–8

[7] Takamura S., Ohno N., Nishijima D. and Kajita S. 2006 Formation of nanostructured tungsten with arborescent shape due to helium plasma irradiation *Plasma Fusion Res.* **1** 051

[8] Baldwin M.J. and Doerner R.P. 2008 Helium induced nanoscopic morphology on tungsten under fusion relevant plasma conditions *Nucl. Fusion* **48** 038001

[9] Kajita S., Yoshida N., Yoshihara R., Ohno N. and Yamagiwa M. 2011 Tem obervation of the growth process of helium nanonbubbles on tungsten: Nanostructure formation mechanism *J. Nucl. Mater.* **418** 152–8

[10] De Temmerman G., Bystrov K., Doerner R.P., Marot L., Wright G.M., Woller K.B., Whyte D.G. and Zielinski J.J. 2013 Helium effects on tungsten under fusion-relevant plasma loading conditions *J. Nucl. Mater.* **438** S78–S83

[11] Miyamoto M. *et al* 2015 Systematic investigation of the formation behavior of helium bubbles in tungsten *J. Nucl. Mater.* **463** 333–6

[12] Ito A.M., Yoshimoto Y., Saito S., Takayama A. and Nakamura H. 2014 Molecular dynamics simulation of a helium bubble bursting on tungsten surfaces *Phys. Scr.* **2014** 014062

[13] Sefta F., Hammond K.D., Juslin N. and Wirth B.D. 2013 Tungsten surface evolution by helium bubble nucleation growth and rupture *Nucl. Fusion* **53** 073015

[14] Dasgupta D., Kolasinski R.D., Friddle R.W., Du L., Maroudas D. and Wirth B.D. 2019 On the origin of fuzz formation in plasma facing materials *Nucl. Fusion* **59** 086057

[15] Hammond K., Blondel S., Hu L., Maroudas D. and Wirth B.D. 2018 Large-scale atomistic simulations of low-energy helium implantation into tungsten single crystals *Acta Mater.* **144** 561–78

[16] Umstadter K.R., Doerner R. and Tynan G. 2009 Effect of bulk temperature on erosion of tungsten plasma-facing components subject to simultaneous deuterium plasma and heat pulses *Phys. Scr.* **2009** 014047

[17] Brezinsek S. and 2015 JET-EFDA contributors. Plasma-surface interaction in the Be/W environment: Conclusions drawn from the JET-ILW for ITER *J. Nucl. Mater.* **463** 11–21

[18] Doerner R.P., Baldwin M.J. and Causey R.A. 2005 Beryllium-tungsten mixed-material interactions *J. Nucl. Mater.* **342** 63–7

[19] Baldwin M.J., Doerner R.P., Nishijima D., Buchenauer D., Clift W.M., Causey R.A. and Schmid K. 2007 Be-w alloy formation in static and divertor-plasma simulator experiments *J. Nucl. Mater.* **363–365** 1179–83

[20] Linsmeier C., Ertl K., Roth J., Wiltner A., Schmid K., Kost F., Bhattacharyya S.R., Baldwin M. and Doerner R.P. 2007 Binary beryllium-tungsten mixed materials *J. Nucl. Mater.* **363–365** 1129–37

[21] Baldwin M.J., Doerner R.P., Nishijima D., Tokunaga K. and Ueda Y. 2009 The effects of high fluence mixed-species (deuterium, helium, beryllium) plasma interactions with tungsten *J. Nucl. Mater.* **390–391** 886–90

[22] Miyamoto M., Nishijima D., Ueda Y., Doerner R.P., Kurishita H., Baldwin M.J., Morito S., Ono K. and Hanna J. 2009 Observations of suppressed retention and blistering for tungsten exposed to deuterium-helium mixture plasma *Nucl. Fusion* **49** 065035

[23] Ueda Y., Fukumoto M., Yoshida J., Ohtsuka Y., Akiyoshi R., Iwakiri H. and Yoshida N. 2009 Simultaneous irradiation effects of hydrogen and helium ions on tungsten *J. Nucl. Mater.* **386–388** 725–8

[24] Ogorodnikova O.V., Sugiyama K., Markin A., Gasparyan Y., Efimov V., Manhard A. and Balden M. 2011 Effect of nitrogen seeding into deuterium plasma on deuterium retention in tungsten *Phys. Scr.* **T145** 014034

[25] Oberkofler M. *et al* 2016 Nitrogen retention mechanisms in tokamaks with beryllium and tungsten plasma-facing surfaces *Phys. Scr.* **T167** 014077

[26] Wood M.A., Cusentino M.A., Wirth B.D. and Thompson A.P. 2019 Data-driven material models for atomistic simulation *Phys. Rev.* B **99** 184305

[27] Plimpton S. 1995 Fast parallel algorithms for short-range molecular dynamics *J. Comput. Phys.* **117** 1–19

[28] Tuckerman M., Berne B.J. and Martyna G.J. 1992 Reversible multiple time scale molecular dynamics *J. Chem. Phys.* **97** 1990–2001

[29] Parrinello M. and Rahman A. 1981 Polymorphic transitions in single crystals: A new molecular dynamics method *J. Appl. Phys.* **52** 7182–90

[30] Stukowski A. 2010 Visualization and analysis of atomistic simulation data with ovito - the open visualization tool *Modelling Simul. Mater. Sci. Eng.* **18** 015012

[31] Juslin N. and Wirth B.D. 2013 Interatomic potentials for simulation of He bubble formation in W *J. Nucl. Mater.* **432** 61–6

[32] Beck D. 1968 A new interatomic potential function for helium *Mol. Phys.* **15** 332

[33] Morishita K., Sugano R., Wirth B.D. and de la Rubia T.D. 2003 Thermal stability of helium-vacancy clusters in iron *Nucl. Instrum. Methods Phys. Res. B* **202** 76–81

[34] Vladimirov P.V. and Moeslang A. 2013 Ab initio static and molecular dynamics studies of helium behavior in beryllium *J. Nucl. Mater.* **442** S694–S698

[35] Borovikov V., Voter A.F. and Tang X.-Z. 2014 Reflection and implantation of low energy helium with tungsten surfaces *J. Nucl. Mater.* **447** 254–70

[36] Hammond K.D. and Wirth B.D. 2014 Crystal orientation effects on helium ion depth distributions and adatom formation processes in plasma-facing tungsten *J. Appl. Phys.* **116** 143301

[37] Hu L., Hammond K.D., Wirth B.D. and Maroudas D. 2015 Molecular-dynamics analysis of mobile helium cluster

reactions near surfaces of plasma-exposed tungsten *J. Appl. Phys.* **118** 163301

[38] Maroudas D., Blondel S., Hu L., Hammond K.D. and Wirth B.D. 2016 Helium segregation on surfaces of plasma-exposed tungsten *J. Phys.: Condens. Matter.* **28** 064004

[39] Was G. 2017 Fundamentals of Radiation Materials Science (Morrisville: Springer)

[40] Boisse J., De Backer A., Domain C. and Becquart C.S. 2014 Modeling of the self trapping of helium and the trap mutation in tungsten using DFT and empirical potentials based on DFT *J. Mater. Res.* **29** 2374–86

[41] Sandoval L., Perez D., Uberuaga B.P. and Voter A.F. 2015 Competing kinetics and He bubble morphology in W *Phys. Rev. Lett.* **114** 105502